ARTICLE   OPEN

Dissolution and precipitation behaviors of zircon under the atmospheric environment

Toru Kitagaki [1] ✉, Kenta Yoshida[2], Pengfei Liu[2] and Takahisa Shobu[3]

The reactive behavior of zircon in three different solutions: 0.1 M HCl (aq), ultrapure water, and 0.1 M NaOH (aq) was examined under normal temperature and pressure conditions. Dissolved Si and Zr concentrations show that considerable Zr precipitated on the surface in all immersion cases. Bulk changes in the zircon were insignificant. However, the obvious surface change of the zircon immersed in 0.1 M NaOH (aq) was confirmed. Porous layer comprising an amorphous SiO_x phase and needle crystals of $ZrSiO_4$ around pores were detected on the near-surface area of the zircon immersed in 0.1 M NaOH (aq). Consequently, the reaction was limited when zircon was immersed in ultrapure water. Zr precipitated on the surface after the dissolution of $ZrSiO_4$ in 0.1 M HCl (aq). Dissolved Zr and Si in 0.1 M NaOH (aq) precipitated on the surface, then the dissolution of $ZrSiO_4$ formed a porous layer, and most dissolved Zr precipitated as zircon crystals.

npj Materials Degradation (2022)6:13 ; https://doi.org/10.1038/s41529-021-00214-0

INTRODUCTION

Zircon, $ZrSiO_4$, is one of the most chemically stable minerals owing to its extreme durability[1]. Various elements are included during zircon crystal growth in a geological environment. Zircon has been used to estimate ancient geological environments by analyzing elements, e.g., absolute dating by U–Pb geochronology, temperature estimation with Ti thermometry, and oxygen potential estimation using valence states of lanthanides[2]. Zircon is also an important material in nuclear engineering: candidate material of the host phase to immobilize Pu[3–5], and one of the main phases containing U in the fuel debris generated by the Chernobyl Nuclear Power Plant unit 4 (ChNPP) accident in 1986[6,7]. The formation of the zircon containing a high amount of U in the fuel debris generated by the Fukushima Daiichi Nuclear Power Station (1F) accident in 2011 was also estimated[8].

During severe nuclear accidents, such as the Three Mile Island Nuclear Generating Station Unit 2 (TMI-2) accident in 1979[9], ChNPP, and 1F, fuel debris is a high-temperature reaction product between nuclear fuels such as U and Pu and structural materials such as zircalloy, SUS, and concrete. Although these accident progressions should be estimated in detail during post-severe accident management to develop other nuclear reactors' safety, the information of the accident environments, such as the measurement data of the spatiotemporal temperature, pressure, and material transport, is too little to estimate the accident progressions in detail. Therefore, estimating accident environments and progression from the situation inside the damaged reactor and the characteristics of the fuel debris is necessary. For example, the maximum reaction temperature during the formation of fuel debris and cooling rate can be estimated from the phases and microstructure of the solidified fuel debris[10]. Moreover, the temporal development of temperature and oxygen potential inside the molten pool generated by the interaction between molten core materials and concrete in primary containment vessel (PCV) can be estimated from the zircon formed in the fuel debris using analytical methods to estimate ancient geological environments[11]. However, the degradation of fuel debris by the reaction with moisture and microbes and the effect of radiation and other factors render it difficult to read the records of the accident progression. Therefore, understanding the degradation behaviors of the fuel debris accumulated in reactors is important to estimate the accident environments and progression. The reaction with moisture is one of the major factors of degradation[12], and the reaction of $(U,Zr)O_2$, which is one of the major phases in fuel debris[7,10,13] with solutions, has been studied to understand the migration behavior of U in the reactors[14,15]. However, the reaction behavior of zircon with solution, which is also one of the matin phases containing high-amount of U in fuel debris, is rarely studied from the point of view of the degradation of fuel debris[11].

The reaction behavior of zircon minerals was classified into two mechanisms: diffusion-reaction mechanism mainly caused in metamict zircon and dissolution-reprecipitation mechanism mainly caused in non-metamict zircon[16]. Metamictization of zircon mainly occurs by the α-decay of the ^{235}U and ^{238}U contained in the zircon. The half-life of ^{235}U and ^{238}U is more than 7×10^8 y. Therefore, the metamictization of the zircon in fuel debris during post-severe accident management is very low during the decommissioning of damaged reactors. It has been reported that as solution temperature exceeds 75 °C[17], zircon in a solution degrades. Herein, we confirmed the surface height changes in zircon in solutions under ordinary temperatures and pressures conditions in a few days using high-resolution phase-shift interferometry[11]. It indicates that zircon dissolves and precipitates in water accumulated in the 1F and ChNPP reactors at normal temperatures and pressures conditions. To understand the reaction behavior of zircon in reactor conditions and evaluate the effect on the estimation of accident environment and progression, the reaction behavior of natural zircon minerals, such as dissolution and precipitation in different acid–base solutions under ordinary temperatures and pressures, was studied.

[1]Collaborative Laboratories for Advanced Decommissioning Science, Japan Atomic Energy Agency, 2-4 Shirakata, Tokai-mura, Ibaraki 319-1195, Japan. [2]International Research Center for Nuclear Materials Science, Institute for Materials Research, Tohoku University, 2145-2, Narita-cho, Oarai-machi, Ibaraki 311-1313, Japan. [3]Materials Sciences Research Center, Japan Atomic Energy Agency, 2-4 Shirakata, Tokai-mura, Ibaraki 319-1195, Japan. ✉email: kitagaki.toru@jaea.go.jp
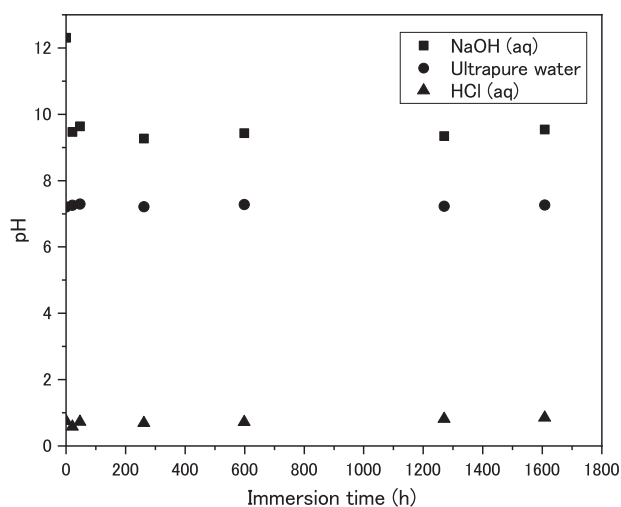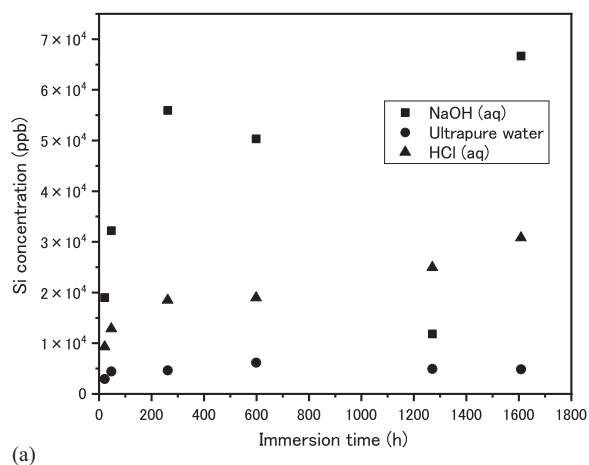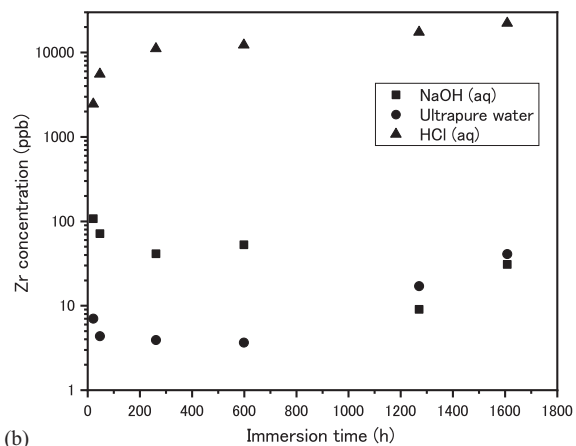
Fig. 1 The pH changes of the solutions of 0.1 M NaOH (aq), ultrapure water, and 0.1 M HCl (aq) in which crushed zircon was soaked.

Fig. 2 The elemental concentration changes in 0.1 M NaOH (aq), ultrapure water, and 0.1 M HCl (aq). **a** The concentrations of Si in 0.1 M NaOH (aq), ultrapure water, and 0.1 M HCl (aq). **b** The concentrations of Zr in 0.1 M NaOH (aq), ultrapure water, and 0.1 M HCl (aq).
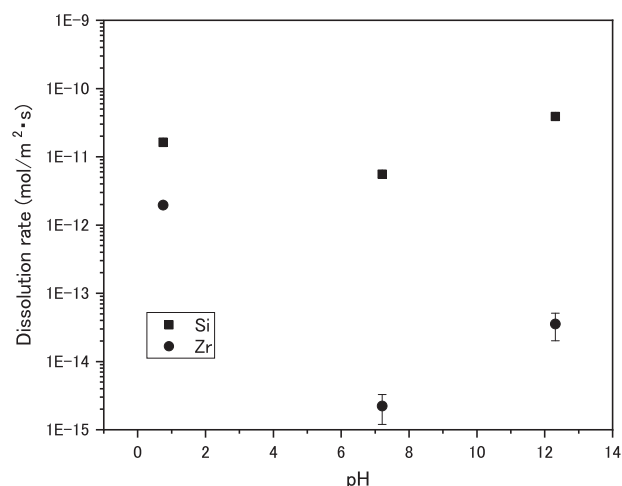

Fig. 3 The dissolution rates of Si and Zr evaluated from the temporal concentration changes in Si and Zr in each solution at the beginning of the immersion. Error bars represent the standard deviation.

RESULTS

Change in the zircon immersing solutions

The pH of the crushed zircon immersing ultrapure water and 0.1 M HCl (aq) was almost constant from the beginning of the immersing, as shown in Fig. 1. Conversely, the pH of 0.1 M NaOH (aq) rapidly decreased to below pH 10 on the first day of the immersion; subsequently, the pH change decreased until the end of the immersion, i.e., after 1608 h. It implies that some reaction occurred at the beginning of the immersion of the zircon powder in 0.1 M NaOH (aq), then it was suppressed.

The concentrations of Si dissolved from the zircon in all three solutions and that of Zr in 0.1 M HCl (aq) increased until approximately 250 h after the zircon was immersed, then they became practically steady or gradually increased, as shown in Fig. 2. Conversely, the concentration of Zr in NaOH (aq) and in ultrapure water remained almost constant during the immersion of zircon. A remarkable feature of the elemental concentrations is the difference between Si and Zr in NaOH (aq). Although the concentration of dissolved Si in NaOH (aq) was the largest in these conditions, the concentration of Zr was approximately 600 times lower than that of Si in the same solution, and it was close to that of Zr in ultrapure water. The dissolution rates of Si and Zr evaluated from the temporal concentration changes in Si and Zr in each solution at the beginning of the immersion (between 0 and 46.5 h) are shown in Fig. 3. The dissolution rates of Si are larger than that of Zr in all cases. It indicates that Zr precipitation after the dissolution of zircon, $ZrSiO_4$, is larger than that of Si.

Change in the bulk of the zircon

X-ray powder diffraction pattern of crushed zircon powder before immersing in solution shows its little metamictization, because the spread of (200) zircon, 2θ is about 27°, which is the distinctive trend in metamictization of zircon[18], is little as shown in Fig. 4. The small changes in the diffraction pattern of the zircon immersed in ultrapure water and HCl (aq) were confirmed. However, the small peak at 32.5° and 38° was established in the diffraction pattern of the zircon immersed in NaOH (aq) as shown in Fig. 4. The peak at 38° is probably NaOH (s) precipitated through drying the NaOH (aq). The peak at 32.5° is insufficient to identify the source of the phase.

The cross-section images of the zircon particles before and after the immersing in each solution measured using synchrotron X-ray microtomography with the energy around Zr K-edge, i.e., 18.0 keV, are shown in Fig. 5. In this image, the more light the region, the
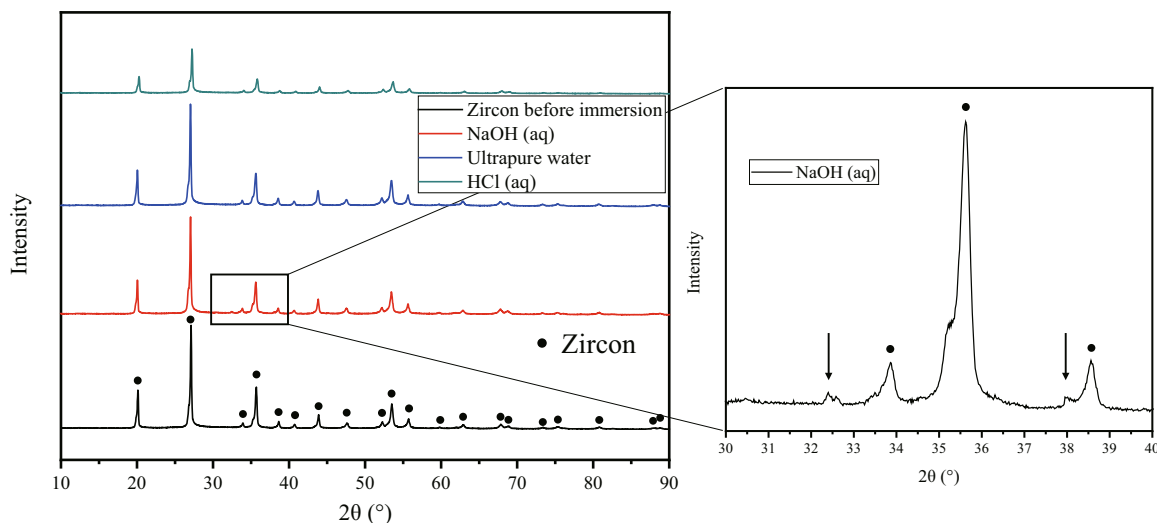
Fig. 4 X-ray powder diffraction pattern of crushed zircon powder before and after immersing in each solution. Left panel shows the pattern before immersion, and after immersing in 0.1 M NaOH (aq), ultrapure water, and 0.1 HCl (aq). Right panel shows unclear peaks at 32.5° and 38° in the pattern after immersing in 0.1 M NaOH (aq).
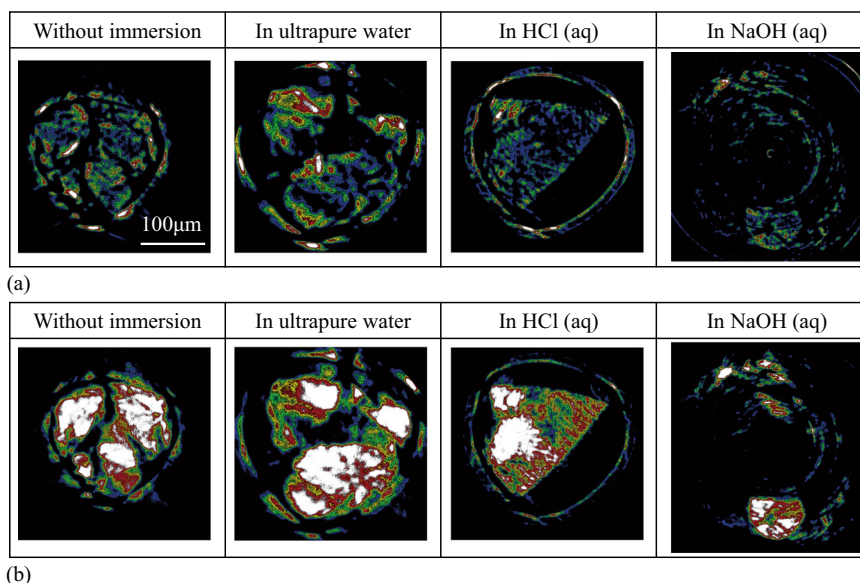

Fig. 5 The cross-section images of the zircon particles before and after the immersing in each solution measured using synchrotron X-ray microtomography with the energy around Zr K-edge. The scale bar is 100 μm. **a** Energy weaker than Zr-K edge (17.9 keV). **b** Energy stronger than Zr-K edge (18.1 keV).

larger the line absorption coefficient, higher the density, or thicker the region. When the energy of the synchrotron X-ray is weaker than Zr K-edge, i.e., 17.9 keV, the images show the distribution of the elements except for Zr. On the other hands, when the energy of the synchrotron X-ray is stronger than Zr K-edge, i.e., 18.1 keV, the images show the distribution of Zr. The inner structure differences between before and after immersing in each solution were minor, indicating that the alterations in the inner structure caused by immersing in the solutions were minor.

These results show that the bulk of the zircon powder changes by immersing in 0.1 M HCl (aq), ultrapure water, and 0.1 M NaOH (aq) for this experimental duration, i.e., 1608 h, are limited.

The surface changes

Figure 6 shows a three-dimensional image of the zircon particles before and after immersion in each solution, as visualized using synchrotron X-ray microtomography at the same energy as the cross-section images above. This Figure's color has the same meaning as Fig. 5. After immersing the samples in 0.1 M HCl (aq) and 0.1 M NaOH (aq), the enrichment of Zr on the surface was confirmed. When immersed in 0.1 M HCl (aq) and 0.1 M NaOH (aq), the surface of the zircon dissolved in the solutions, and a substantial amount of dissolved Zr precipitated on the surface of the particles.

The results of the surface observation of the zircon using SEM show no obvious change on the surface of the zircon after immersing in 0.1 M HCl (aq) and ultrapure water. Alternatively, the several micrometers-long needle crystals were confirmed on the zircon's surface immersed in 0.1 M NaOH (aq), as shown in Fig. 7. Therefore, the surface modification of the zircon after immersing in 0.1 M NaOH (aq) was evaluated in detail as mentioned below.

Without immersion	In ultrapure water	In HCl (aq)	In NaOH (aq)

(a)

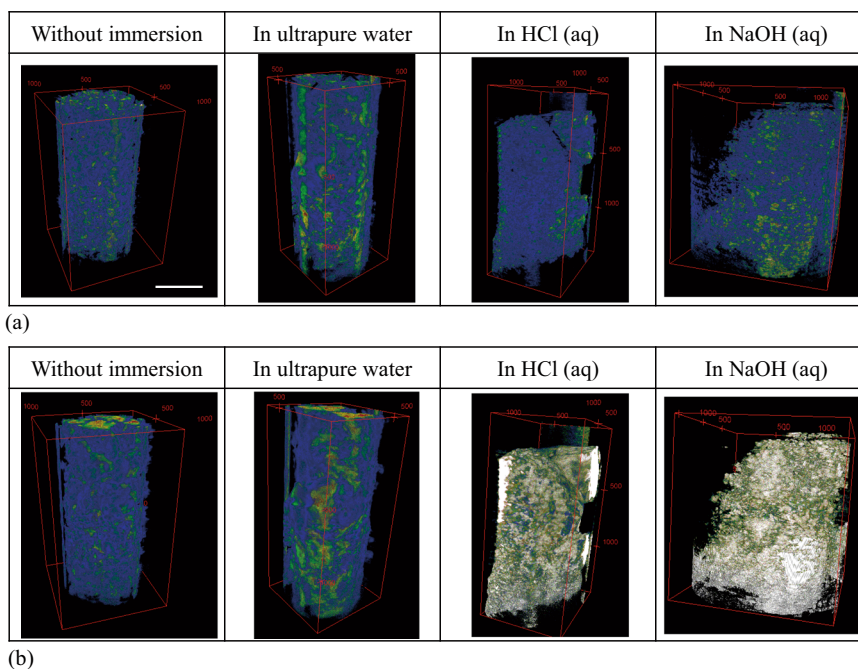| Without immersion	In ultrapure water	In HCl (aq)	In NaOH (aq)

(b)

Fig. 6 The three-dimensional image of the zircon particles before and after immersion in each solution measured using synchrotron X-ray microtomography with the energy around Zr K-edge. The scale bar is 100 µm. **a** Energy weaker than Zr-K edge (17.9 keV). **b** Energy stronger than Zr-K edge (18.1 keV).
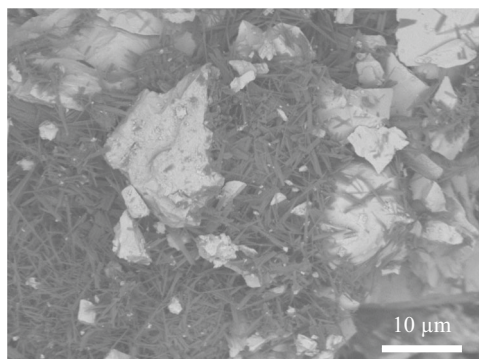
Fig. 7 The back scattering image of the surface of the zircon particle immersed in 0.1 M NaOH (aq). The scale bar is 10 µm.
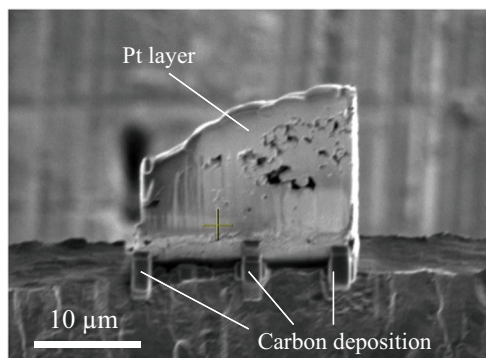
Fig. 8 Cross-sectional secondary electron image of the zircon immersed in 0.1 M NaOH (aq). The scale bar is 10 µm.

The several micrometer depth ranges of the zircon surface were hewed out from the zircon immersed in 0.1 M NaOH (aq) using focused ion beam (FIB) micro-sampling technique, as shown in Fig. 8. This figure confirms that the Pt layer was coated on the surface of the piece to avoid the irradiation damage by Ga ion beam. Several micrometers of many pores can be observed near the interface of the zircon piece. FIB sliced the piece into a thin film with a thickness of 150 nm to analyze the detail nanostructure and chemical composition by an 200 kV aberration corrected (scanning) transmission electron microscopy (AC-(S)TEM) with an energy dispersive X-ray spectroscopy (EDS). In Fig. 9, the presence of rod-shaped materials around pores was discovered without exception in the three FIB samples. Bright-field (BF) STEM images are recorded with a probe semi-angle of 5.2 mrad and selective detection angle of 8.0 mrad has successfully visualized diffraction contrast inner surface of the zircon piece with large field-of-view above 10×10 mm^2 and long depth of field 500 nm[19]. Red arrows in BF-STEM images indicate such rod-shaped materials. The dark contrasts of the rod-shaped materials were sensitively changed with an objective lens defocus and sample orientation. This result means that the rod-shaped material is crystal, hereafter referred to as a needle crystal.

The intensity of the region surrounding pores are relatively higher than on of the needle crystal. Therefore, the materials surrounding pores are amorphous. The HAADF–STEM images of the same region as the BF-STEM images are shown in Fig. 10. The heavier elements appear like brighter images. The needle crystal is bright, and these are heavy elements. The zircon comprises Zr, Si, O, and NaOH (aq) is H, O, and Na. Zr is the heaviest element in this system, indicating that the needle crystal is a Zr-rich material. The elemental mapping using the EDS of the same region as the BF-STEM and HAADF–STEM images are shown in Fig. 11. The needle crystals comprise Zr, Si, and O. This result corresponds to the HAADF–STEM images. The region surrounding pores are Si-rich oxide materials, and it indicates that this region is a Si-rich amorphous oxide.
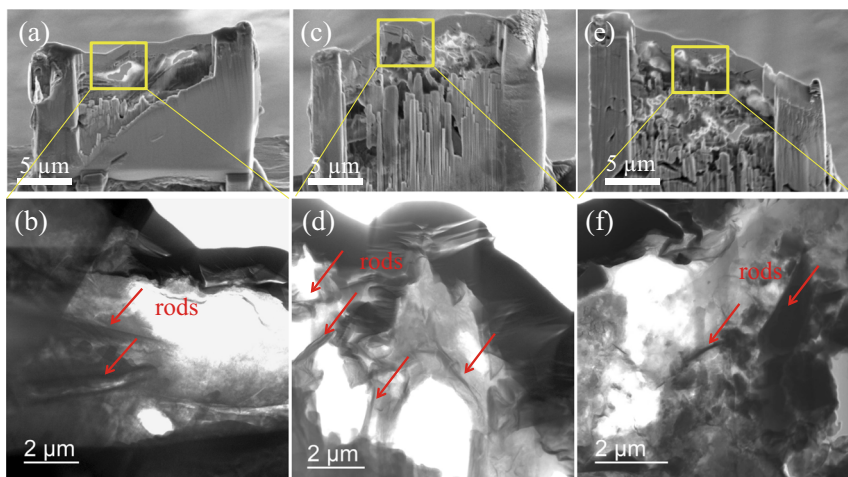
Fig. 9 BF-TEM and BF-STEM images of thin films fabricated from the zircon surface immersed in NaOH (aq). a, **c**, **e** Low-magnification BF-TEM images of 150 nm thin films fabricated from the zircon immersed in NaOH (aq). **b**, **d**, **f** High-magnification BF-STEM images obtained from square surrounded area in low-magnification images, respectively. The scale bar on the upper three images is 5 μm, the bottom is 2 μm.

The zircon powder was crushed using an agate mortar in 2-propanol for the analysis using high-resolution TEM (HRTEM) and electron diffraction (ED) to identify the phase of the needle crystal. Figure 12a is a low-magnification TEM bright-field image of the micrometers-long needle crystal. The needle crystal was identified as single crystalline zircon (space group number 141) using HRTEM shown in Fig. 12b along the [021] direction, in addition to an ED pattern obtained with a selected area aperture of 300 nm in diameter, as shown in Fig. 12c. The ED pattern of the other region close to the needle crystal shown in Fig. 13 shows that this region is an amorphous material. Therefore, this region is amorphous SiO_x.

DISCUSSION

When zircon powder was immersed in ultrapure water under an ordinary atmosphere, dissolved Si and Zr were limited. The concentration of Si in ultrapure water was approximately 10^3 times larger than that of Zr, and it indicated that most Zr precipitated after the dissolution of $ZrSiO_4$. The obvious bulk change was small, and the obvious change of the surface was also limited. The decrease in the surface height of the zircon under a similar condition was confirmed[11]. It indicates that the surface of the zircon in ultrapure water was gradually dissolved, then most Zr precipitated on the surface. This precipitation was insufficient to prevent continuous dissolution.

In the case of the zircon immersed in 0.1 M HCl (aq), although the change in the bulk of the zircon was small, the enrichment of Zr on the surface of the zircon was confirmed using synchrotron X-ray microtomography. The concentration of dissolved Si was approximately twice larger than that of Zr. The decrease in the surface height of the zircon and a large amount of precipitation on the surface under immersion in 1 M HCl (aq) were confirmed[11]. Consequently, the dissolution of zircon in 0.1 M HCl (aq) is relatively fast compared to the other conditions, and at least half Zr precipitate on the surface. However, the prevention of the dissolution by the precipitations is limited because the adhesion of the precipitates on the surface is limited[11].

In the zircon immersed in 0.1 M NaOH (aq), an immediate decrease in pH and the evaluated dissolution rate of Si and Zr indicate that the dissolution of $ZrSiO_4$ in NaOH (aq) is the fastest in the studied range, and most Zr precipitates on the surface. Moreover, this precipitation of Zr restricts the additional dissolution of the zircon. The dissolution of $ZrSiO_4$ makes a porous layer to a depth of several micrometers from the surface, and most

dissolved Zr precipitates as zircon needle crystals. At this time, the small peak of NaOH (s) in X-ray diffraction patter of the zircon immersed in 0.1 M NaOH (aq) indicates that the part of needle-like material confirmed in Fig. 7 is NaOH (s) which was generated by drying of NaOH (aq). The part of Si also precipitates in this porous layer as an amorphous oxide, SiO_x. This result suggests that these phenomena are one of the reasons for the durability of the zircon. Similar phenomena were also confirmed with the reaction between the zircon with high-temperature solutions[16]. This study shows that similar phenomena can occur under atmospheric environments.

Many zircon crystals, including several molar percentages of U, were founded in the lava-like fuel-containing materials (LFCM) of ChNPP[6,7]. However, the obvious degradation of the zircon was not confirmed because the water from rainfall accumulates in the bottom region of the sarcophagus of ChNPP, and the zircon containing LFCM samples were picked up from the upper region. Some LFCM were immersed in the accumulated water, and there is a possibility that the zircon was dissolved in the accumulated water with the other part of LFCM. The accumulated water was contaminated by the dissolution of radioisotope such as Cs, Sr, Pu, and Am[20]. The pH of the accumulated water in the sarcophagus is approximately 9, and carbonate ions and other anions were detected[20]. Therefore, when zircon is immersed in accumulated water, the zircon dissolves from the surface, and a porous layer comprising Si amorphous oxides and $ZrSiO_4$ needle crystal is formed. The depth of the reacted layer of the zircon depends on the pH of the accumulated water and the duration of the immersion in the sarcophagus. The effect of carbonate ions and another anion on the degradation should be considered in case of actual environment. The dissolution of UO_2 is accelerated by carbonate ions[21]. Therefore, zircon containing U can also be accelerated. This modification of the outer region of the zircon eliminates the part of the accident record. The comparison between the zircon immersed in the accumulated water and the zircon without or less reaction with the accumulated water in the sarcophagus of ChNPP provides detailed understanding of the reaction behavior of zircon with water under an ordinary atmosphere. Moreover, the effect of U contained in the zircon and radiolysis generated by the radiation of the water can be evaluated.

It was predicted that zircon was included in the molten core concrete interaction (MCCI) caused in the PCVs during the 1F accident[8]. The pure cooling water filtered contaminated water using reverse osmosis membrane and other filtering systems has
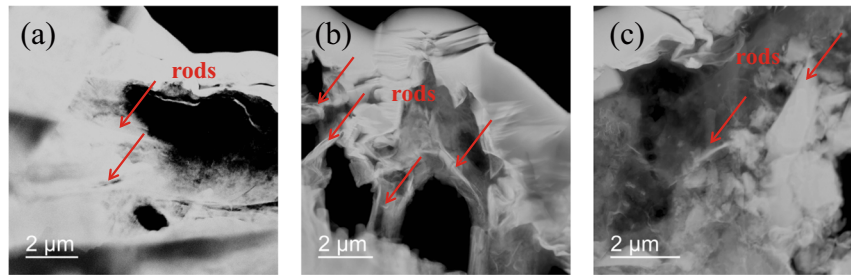
Fig. 10 HAADF-STEM images of the zircon sample thin films with inner/outer detection angle of 110–440 mrad. The scale bar is 2 µm.
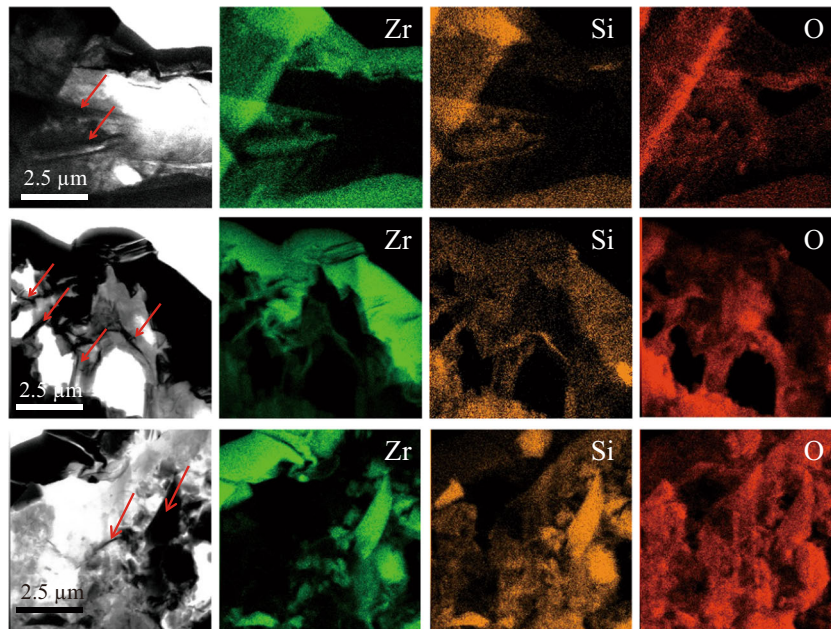

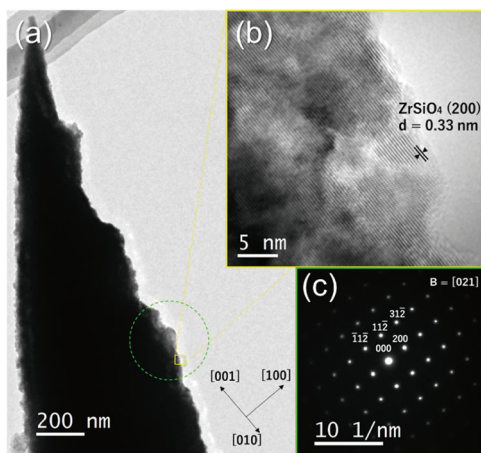**Fig. 11 The elemental mapping by EDS near the surface of the zircon.** The scale bar is 2.5 µm.

Fig. 12 TEM images and SAED pattern of the rod crystal. a Bright-field TEM image of the rod crystal, **b** HRTEM image, and **c** SAED pattern. The scale bar on the left image is 200 nm, the upper right is 5 nm and the bottom right, 10 nm^{-1}.

been injected in the reactors, and the fuel debris accumulated in the PCV is immersed in the water[22]. It was confirmed that the radionuclides are eluted in the water from the fuel debris[23]. The pH of the water accumulated in the PCVs is 6.6–7.4[24]. Therefore,

the reaction behavior of zircon in the MCCI product with the accumulated water is similar to that of the zircon with ultrapure water evaluated herein. The reaction of zircon with ultrapure water is limited.

Moreover, the zircon was covered by other phases, such as amorphous/crystalline SiO_2 phases generated by melting and cooling of reacted concrete with molten core materials. Therefore, only a limited part of the zircon contacts with the water under 1F conditions. Above all, it is concluded that the effect of the degradation of zircon in the fuel debris of 1F to the estimation of 1F accident progression is limited. Moreover, analyzing the degradation behavior of zircon and other phases in the fuel debris and evaluating the differences of the degradation behavior between laboratory conditions and the internal reactor conditions is useful to evaluate the degradation behavior of zircon under atmospheric environment, even for fuel debris during storage or geological disposal.

METHODS

Zircon specimen and immersing condition

The piece of the (101) plane of the zircon mineral from Malawi was crushed to less than 70 µm using a tungsten motar, and it was immersed in three different solutions; 0.1 M HCl (aq), ultrapure water, and 0.1 M NaOH (aq). The immersing conditions were the following. The weight of the zircon powder in each solution was 0.5 g (specific surface area: 2.574 m^2 g^{-1}). The solution volume was 7 ml. The vessel made of teflon was used. The
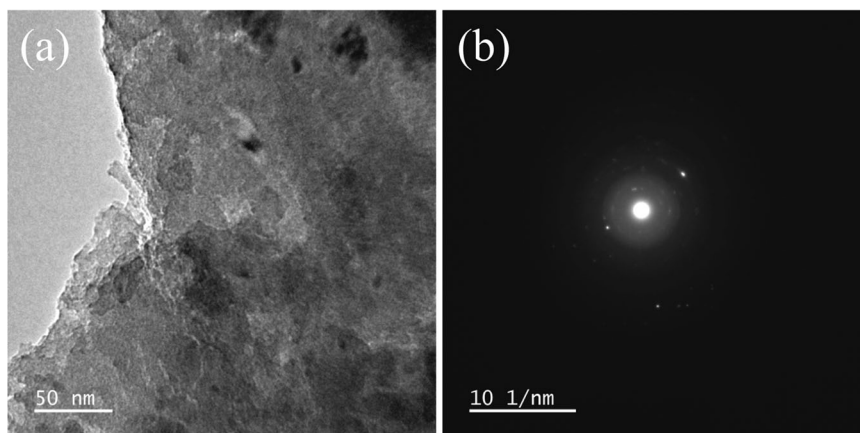
Fig. 13 TEM images and SAED pattern of amorphous region. a Bright-field TEM image, **b** SAED pattern, obtained from amorphous region of the zircon immersed in 0.1 M NaOH (aq). The scale bar on the left image is 50 nm, the right is 10 nm^{-1}.

temperature was kept at 30 °C in thermostatic oven. The maximum immersing duration was 67 days (1608 h). The samples of the solutions for analysis were picked up from the different solutions adjusted under the same conditions. The concentrations of Si and Zr were measured using inductively coupled plasma mass spectrometry. Dissolution rate, rate, was calculated as below.

$$\text{Rate} = \frac{k \times V_{\text{cell}}}{\text{SSA} \times m_{\text{zircon}} \times n_{\text{Si,Zr}}}, \tag{1}$$

where rate represents molar flux (mol m^{-2} s^{-1}); k denotes the slope of time versus concentration of Si or Zr (mol l^{-1} s^{-1}): the concentrations of Si or Zr at 21.5 and 46.5 h after immersing the solutions were used to evaluate initial dissolution behavior; V represents solution volume (l); SSA denotes the specific surface area of zircon; m_{zircon} represents the mass of zircon (g); and $n_{\text{Si,Zr}}$ denotes the stochiometric number of Si and Zr, i.e., 1.0 and 1.0, respectively.

Bulk analysis

The crystal structures of the zircon powder before and after immersing in solutions were identified using powder X-ray diffraction (D2 PHASER, Bruker). Synchrotron X-ray microtomography was carried out at JAEA beamline BL22XU in SPring-8. The X-rays are monochromatized by a Si (111) double-crystal monochromator. In order to emphasize Zr, X-ray microtomography measurements were made with two energies, 17.9 and 18.1 keV, which are the energies before and after the X-ray K absorption edge of Zr. Transmission and direct X-ray images were recorded with a visible-light conversion type X-ray camera which consisted of a powder CsI scintillator, relay lenses and a complementary metal oxide semiconductor (CMOS) camera. The CMOS camera used in the experiments is an ORCA-Flash4.0 (Hamamatsu Photonics K.K.), which has 2048 × 2048 pixels and a field of view (FOV) of 0.666 mm × 0.666 mm. The number of projection images in a half rotation of the samples was fixed to 600. The image reconstruction was performed by the software developed by SPring-8[25].

Surface analysis

The surface conditions of the zircon specimens were evaluated from the backscattering images of the zircon surface measured using field emission SEM (JSM-7900F, JEOL).

The local structure and chemical composition near surface of the zircon particle were characterized using FIB micro-sampling technique (Helios FIB-SEM, Thermo Fisher Scientific) and advanced analytical TEM/STEM (spherical aberration corrected ARM 200F, JEOL)[26] with silicon drift X-ray detector in nanometer scale.

The crystal structure of the typical regions on the needle was identified by selected area electron diffraction (SAED) and high-resolution transmission electron microscopy (HRTEM) in an atomic scale[27].

DATA AVAILABILITY

All relevant data are available from the authors of this paper.

REFERENCES

1. Hanchar, J. M. & Miller, C. F. Zircon zonation patterns as revealed by cathodoluminescence and backscattered electron images: implications for interpretation of complex crustal histories. *Chem. Geol.* **110**, 1–13 (1993).
2. Harley, S. L. & Kelly, N. M. Zircon tiny but timely. *Elements* **3**, 13–18 (2007).
3. Gentry, R. V. et al. Differential lead retention in zircons: implications for nuclear waste containment. *Science* **216**, 296–298 (1982).
4. Ewing, R. C., Lutze, W. & Weber, W. J. Zircon: A host-phase for the disposal of weapons plutonium. *J. Mater. Res.* **10**, 243–246 (2011).
5. Burakov, B. E., Ojovan, M. I. & Lee, W. E. *Crystalline Materials for Actinide Immobilisation*. Vol. 1 (Imperial College Press, 2011).
6. Anderson, E. B., Burakov, B. E. & Pazukhin, E. M. High-uranium zircon from "Chernobyl Lavas". *Radiochim. Acta* **60**, 149–151 (1993).
7. Pazukhin, É. M. Fuel-containing lavas of the Chernobyl NPP fourth block: topography, physicochemical properties, and formation scenario. *Radiochemistry* **36**, 97–142 (1994).
8. Kitagaki, T., Yano, K., Ogino, H. & Washiya, T. Thermodynamic evaluation of the solidification phase of molten core-concrete under estimated Fukushima Daiichi nuclear power plant accident conditions. *J. Nucl. Mater.* **486**, 206–215 (2017).
9. Mccardell, R. K., Russell, M. L., Akers, D. W. & Olsen, C. S. Summary of TMI-2 core sample examinations. *Nucl. Eng. Des.* **118**, 441–449 (1990).
10. Hofmann, P. Current knowledge on core degradation phenomena, a review. *J. Nucl. Mater.* **270**, 194–211 (1999).
11. Kitagaki, T. Evaluation of the dissolution behavior of zircon using high-resolution phase-shift interferometry microscope. *J. Nucl. Mater.* **557**, 153254 (2021).
12. Shiryaev, A. A. et al. Physico-chemical properties of Chernobyl lava and their destruction products. *Prog. Nucl. Energy* **92**, 104–118 (2016).
13. Cohen, I. & Schaner, B. E. A metallographic and x-ray study of the UO$_2$-ZrO$_2$ system. *J. Nucl. Mater.* **9**, 18–52 (1963).
14. Kumagai, Y., Takano, M. & Watanabe, M. Reaction of hydrogen peroxide with uranium zirconium oxide solid solution-zirconium hinders oxidative uranium dissolution. *J. Nucl. Mater.* **497**, 54–59 (2017).
15. Sasaki, T., Takeno, Y., Kobayashi, T., Kirishima, A. & Sato, N. Leaching behavior of gamma-emitting fission products and Np from neutron-irradiated UO$_2$-ZrO$_2$ solid solutions in non-filtered surface seawater. *J. Nucl. Sci. Technol.* **53**, 303–311 (2015).
16. Geisler, T., Schaltegger, U. & Tomaschek, F. Re-equilibration of zircon in aqueous fluids and melts. *Elements* **3**, 43–50 (2007).
17. Geisler, T., Zhang, M. & Salje, E. K. H. Recrystallization of almost fully amorphous zircon under hydrothermal conditions: an infrared spectroscopic study. *J. Nucl. Mater.* **320**, 280–291 (2003).
18. Murakami, T., Chakoumakos, B. C. & Ewing, R. C. In *Advances in Ceramics Vol. 26 (Nuclear Waste Management II)* 745–753 (American Ceramic Society, 1986).
19. Yoshida, K. et al. Weak-beam scanning transmission electron microscopy for quantitative dislocation density measurement in steels. *Microscopy* **66**, 120–130 (2017).

20. Odintsov, O. O., Khan, V. E., Krasnov, V. O. & Shcherbin, V. M. Long term monitoring of the unorganized accumlationsliquid radioactive waters of object «UKRYTTYA». *Probl. Nucl. Saf. Chernobyl.* **27**, 43–57 (2016).
21. Gorman-Lewis, D., Burns, P. C. & Fein, J. B. Review of uranyl mineral solubility measurements. *J. Chem. Thermodyn.* **40**, 335–352 (2008).
22. Nakayoshi, A. et al. Review of Fukushima Daiichi Nuclear Power Station debris endstate location in OECD/NEA preparatory study on analysis of fuel debris (PreADES) project. *Nucl. Eng. Des.* **369**, 110857 (2020).
23. Koma, Y. & Murakami, E. Contamination of Fukushima Daiichi Nuclear Power Station with actinide elements. *Radiochim. Acta* **107**, 965–977 (2019).
24. *Fukushima Daiichi Radwaste Analytical Data Library (FRAnDLi).* https://frandli-db.jaea.go.jp/FRAnDLi/return.php.
25. *Computed Tomography in SPring-8 (SP-μCT).* http://www-bl20.spring8.or.jp/xct/index-e.html.
26. Haider, M., Braunshausen, G. & Schwan, E. Correction of the spherical aberration of a 200 kV TEM by means of a hexapole-corrector. *Optik* **99**, 167–179 (1995).
27. Williams, D. B. & Carter, C. B. *Transmission Electron Microscopy* (Plenum, 1996).

AUTHOR CONTRIBUTIONS

T.K. conceived the conception of the research, performed laboratory tests and analysis, interpreted the results along with contributions by all authors, wrote the manuscript with contributions by all authors. K.Y. and P.L. designed and performed the analysis using TEM/STEM. T.S. designed and performed the experimental work using synchrotron X-ray tomography at SPring-8.

COMPETING INTERESTS

The authors declare no competing interests.

ADDITIONAL INFORMATION

Correspondence and requests for materials should be addressed to Toru Kitagaki.

Reprints and permission information is available at http://www.nature.com/reprints

Publisher's note Springer Nature remains neutral with regard to jurisdictional claims in published maps and institutional affiliations.